Electrochimica Acta 377 (2021) 138071

Contents lists available at ScienceDirect

Electrochimica Acta

journal homepage: www.elsevier.com/locate/electacta

Photoelectrocatalytic detection of NADH on n-type silicon semiconductors facilitated by carbon nanotube fibers

Melisa del Barrio[a,b,*], Moumita Rana[c], Juan José Vilatela[c], Encarnación Lorenzo[b,d], Antonio L. De Lacey[a], Marcos Pita[a,*]

[a] Instituto de Catálisis y Petroleoquímica, CSIC, C/ Marie Curie 2, Madrid 28049, Spain
[b] Departamento de Química Analítica y Análisis Instrumental, Universidad Autónoma de Madrid, Ciudad Universitaria de Cantoblanco, Madrid 28049, Spain
[c] IMDEA Materials Institute, C/ Eric Kandel 2, Getafe, Madrid 28906, Spain
[d] IMDEA-Nanociencia, Ciudad Universitaria de Cantoblanco, Madrid 28049, Spain

ARTICLE INFO

Article history:
Received 17 December 2020
Revised 22 February 2021
Accepted 28 February 2021
Available online 4 March 2021

keywords:
NADH detection
Photoelectrochemistry
Carbon nanotube fibers
Semiconductor

ABSTRACT

NADH is a key biomolecule involved in many biocatalytic processes as cofactor and its quantification can be correlated to specific enzymatic activity. Many efforts have been taken to obtain clean electrochemical signals related to NADH presence and lower its redox overpotential to avoid interferences. Suppression of background and secondary signals can be achieved by including a switchable electroactive surface, for instance, by using semiconductors able to harvest light energy and drive the excited electrons only when irradiated. Here we present the combination of a n-type Si semiconductor with fibers made of carbon nanotubes as electroactive surface for NADH quantification at low potentials only upon irradiation. The resulting photoelectrode responded linearly to NADH concentrations from 50 μM to 1.6 mM with high sensitivity (54 μA cm^{-2} mM^{-1}). This system may serve as a biosensing platform for detection and quantification of dehydrogenases' activity.

© 2021 The Author(s). Published by Elsevier Ltd.
This is an open access article under the CC BY-NC-ND license
(http://creativecommons.org/licenses/by-nc-nd/4.0/)

1. Introduction

Nicotinamide adenine dinucleotide (NAD) and its reduced form (NADH) are an important redox couple found in all living systems. They act as enzymatic cofactors and play a key role in biological electron transport. NADH is involved in the reactions catalysed by more than 300 dehydrogenase enzymes [1], in ATP synthesis, and also other non-redox processes such as repairing the DNA system [2,3]. Moreover, altered NADH levels are linked to various neurodegenerative diseases [4–7] and mental disorders [4,8,9]. Given its biochemical and medical interest, several methods have been employed to detect NADH, including high performance liquid chromatography [10], fluorescence [11,12], electrochemiluminesce [13–15], electrochemical [3,16,17], and photoelectrochemical [18–24] methods.

In the last decades, research efforts have been focused on the electrochemical oxidation of NADH to NAD^+ [25,26] due to the advantages of electrochemical detection, such as simple instrumentation and high sensitivity. Although the formal redox potential of the NAD^+/NADH couple is −0.320 V vs. NHE, NADH shows slow electron transfer kinetics at unmodified electrodes and overpotentials larger than 1 V need to be applied for the oxidation of the analyte, which increases the risk of interferences. Fouling of the electrode surface due to the adsorption of oxidation products, which leads to electrode passivation and therefore irreproducibility of the analytical signal, has also been observed [1,27]. To overcome the problems of bare electrodes, the modification of the electrode surface with redox mediators (e.g. quinone derivatives, phenazine, phenoxazine and phenothiazine dyes, nitro-fluorenone and catechol) which catalyze the oxidation of NADH [17,28,29], polymers [3], and nanomaterials, such as carbon nanotubes and graphene sheets [16], have been widely considered. Physical adsorption, electropolymerized films, and to a lesser extent, covalent attachment have been used for the electrode modification with redox mediators to obtain a stable immobilization. Carbon nanotubes show electrocatalytic activity towards NADH oxidation and minimize surface fouling, but these carbon nanomaterials have low solubility and, consequently, involve tedious protocols for electrode modification. Preliminary results on electrocatalytic NADH oxidation on carbon nanotube fiber microelectrodes were reported by Wang et al.

* Corresponding authors.
E-mail addresses: melisa.delbarrio@uam.es (M. del Barrio), marcospita@icp.csic.es (M. Pita).

https://doi.org/10.1016/j.electacta.2021.138071
0013-4686/© 2021 The Author(s). Published by Elsevier Ltd. This is an open access article under the CC BY-NC-ND license
(http://creativecommons.org/licenses/by-nc-nd/4.0/)

[30], and only some optimizations have been proposed since then by the use of redox mediators and specific pretreatments [31].

More recently, photoelectrochemical (PEC) detection methods have become very popular due to their attractive advantages. They inherit the benefits of electrochemical detection and represent a highly sensitive and low background signal approach, as they use a unique signal transducing modality involving separate processes for signal generation (photoexcitation) and detection (electrochemical) [32]. PEC biosensing devices have been applied in nucleic acid analysis, immunoassays, cell detection, protein/enzyme sensing, and the monitoring of small molecules [33–36], such as those that are produced during enzymatic reactions (e.g. oxygen, hydrogen peroxide, or NADH). Semiconductors are key components of PEC systems, as they allow the switching ON and OFF upon illumination [33,35]. Most PEC sensors found in the literature are based on quantum dots (QDs) and TiO_2 [37], often combined with other photoactive materials to improve their PEC behavior. For instance, traditional QDs (e.g. CdSe and CdS) exhibit low photon-to-current conversion efficiencies, due to their relatively low quantum yields, and are prone to photobleaching, which results in unstable photocurrents. Therefore, QDs-based PEC platforms include other semiconducting materials, like graphitic carbon nitride or metallic oxides [33]. Furthermore, a new class of QDs, $CsPbBr_3$ perovskite QDs, exhibited better PEC characteristics and was used, in combination with ZnO inverse opal photonic crystals, for NADH detection [18]. Nevertheless, the toxicity of the metal ions from QDs (Cd, Se, Pb…) and the poor stability of perovskite are still an issue. Regarding TiO_2 nanoparticles, apart from being subject to some of the problems previously indicated for QDs, they can only use UV light for due to the inherent band gap of this semiconductor, which limits their applications. The construction of heterostructured TiO_2 photoelectrodes by coupling this material with another semiconductor having a smaller band gap or a dye sensitizer have been proposed to overcome this issue [37]. The generation of a Ti-dopamine charge transfer complex was used for the design of the only TiO_2 photoelectrode reported for PEC sensing of NADH under visible irradiation [23].

Here we show the photocatalytic detection of NADH at low potential on a simple platform composed of a n-type silicon semiconductor and a carbon nanotube fiber film (Si/CNT_f). Si has a small band gap of 1.1 eV, which enables visible-light-driven oxidation reactions. Carbon nanotube fibers were easily deposited on the semiconductor surface without further modifications with any redox mediator. In spite of the unique properties of this carbon nanomaterial, such as excellent conductivity, high surface area and stability [38,39], they have barely been exploited for NADH determination. First, we characterize both CNT_f and Si/CNT_f photoelectrodes by scanning and transmission electron microscopy, Raman and impedance spectroscopy. Then, we show the photocatalytic oxidation of NADH on Si/CNT_f photoelectrodes and we investigate the origin of the photooxidation signal. Furthermore, the analytical performance and stability of the photoelectrodes are evaluated.

2. Experimental

2.1. Reagents

Sodium hydrogen phosphate, sodium dihydrogen phosphate dihydrate, β-nicotinamide adenine dinucleotide reduced disodium salt hydrate (NADH), n-type silicon ⟨111⟩ wafers doped with phosphorous, fluorine-doped tin oxide (FTO) coated glasses, potassium ferricyanide, potassium ferrocyanide trihydrate, ferrocene, thiophene, and toluene were purchased from Merck. 3-Aminopropyltriethoxysilane 99% (APTES) and toluene 99.9% were obtained from Fisher Scientific. Grey dielectric paste was supplied by Gwent Group. Fresh MilliQ-grade water purified with Millipore filtering system water (18.2 Ω cm) was used to prepare aqueous solutions.

2.2. Instruments

Photoelectrochemical measurements were performed in a three-electrode cell configuration using a Pt wire as a counter electrode and an Ag/AgCl (3 M NaCl) reference electrode. The cell was filled with 5 mL of 100 mM phosphate buffer pH 7.4. The measurements were carried out at room temperature and controlled with a microAutolab II potentiostat from Metrohm. Illumination was carried out with a LOT Quantum Design 150 W Xenon lamp with the output power set to 81 W, so that the power reaching to the electrode surface corresponded approximately to one average Sun intensity. A 1 mm-thick polycarbonate UV filter was used to absorb the radiation below ≈380 nm. Electrochemical impedance spectroscopy (EIS) experiments were performed in an equimolar $[Fe(CN)_6]^{4-}/[Fe(CN)_6]^{3-}$ solution (0.5 mM each in phosphate buffer) at 0.2 V vs Ag/AgCl by applying an alternating current (AC) amplitude of 10 mV in a frequency range from 10^4 to 0.1 Hz, using an Autolab PGSTAT30/FRA2 potentiostat/galvanostat from Metrohm. EIS data was fitted using electrical equivalent circuits with ZView2 software from Scribner Associates Inc. (USA). The microscopic structure of the CNT fibers were investigated using field emission scanning electron microscopy (FESEM, Helios Nanolab 600i FIB-FEGSEM dual-beam microscope, at 5 kV) and transmission electron microscopy (TEM, Talos F200X FEG, 80 kV). Raman spectroscopy measurements were performed using a Renishaw microspectrometer equipped with a He−Ne laser (532 nm wavelength)Thermogravimetric analysis (TGA) was performed using a Q50 thermobalance from TA Instruments under aerial condition. Wetting was analysed by determining spreading rate and equivalent contact angle through image analysis of liquid drops on porous CNT fiber samples, as described previously [40].

2.3. Preparation of carbon nanotube fibers (CNT_f)

To synthesize the CNT fibers, a floating catalyst chemical phase vapor deposition (FC–CVD) process was used where toluene, ferrocene and thiophene as carbon, catalysts and promoter sources, respectively. The precursors were injected continuously from the top of a vertical tube furnace maintaining a temperature of 1250 °C under H_2 atmosphere to produce aerogel of long CNTs floating in the gas phase. The continuous fibers of CNT were mechanically withdrawn at the bottom of the tube furnace and winded on a rotating spool leading to a unidirectional non-woven fabric.

2.4. Preparation of the Si/CNT_f photoelectrodes

The procedures for cleaning and silanizing the silicon wafers were adapted from a previous work using a different silane coupling agent [41]. Silicon wafers were cut into 0.8 × 2 cm chips and cleaned by immersing them in a solution composed of 1:1:1 ammonium hydroxide (30%), hydrogen peroxide (30%) and water at 60 °C for 1 h. Then the chips were rinsed with water and dried with an Ar stream. The surface was then modified with a 2% APTES solution in dry toluene for 15 min at 60 °C. The silanized surface was sequentially rinsed with toluene, ethanol and water and dried in an oven at 110 °C. The CNT_f were deposited as reported before [42]. First, the CNT_f, covered on both sides by protective plastic sheets, were cut into 0.5 × 0.5 cm pieces using scissors. After removing the plastic sheet, one piece was placed on the surface of Si electrodes with the help of PTFE tweezers. Finally, a drop of acetone was added, wetting the CNT_f, while the edges of the piece were held to prevent the piece getting folded or rolled up. A flat and well attached layer was obtained. Afterwards, the electrodes

were heated at 150 °C. This thermal treatment, together with the Si modification with the silanization agent (APTES) improved the charge transfer and the stability of the photoresponse. Finally, the exposed Si surface of the electrode was completely masked with PTFE tape, except for a small area (width = 1 mm) around the CNT_f.

2.5. Preparation of FTO/CNT_f photoelectrodes

FTO-covered glasses were cut into 2 × 3 cm slides and cleaned as reported in [43], by sequentially immersing them in water, ethanol and acetone in an ultrasonic cleaner for 15 min. Afterward, the slides were let to dry. A copper wire was fixed to one edge of the FTO surface with conductive adhesive tape. A 1 cm diameter piece of CNT_f was then placed on the FTO surface by following the procedure described in the previous section for Si electrodes. The FTO electrode was then masked with dielectric paste.

3. Results and discussion

3.1. Characterization of the photoelectrodes

Due to their inherent hydrophobic nature, the as-prepared CNT_f fabric can hardly interact with the aqueous electrolytes. Therefore, to improve their hydrophilicity the pristine fibers were exposed to ozone, generated in situ from a UV source under aerial atmosphere for 30 min each side [44]. This helps in oxidizing the CNT surface, as observed by the Raman spectroscopy. Fig. 1a shows the comparison of the Raman spectra of the pristine CNT_f with the ones treated with ozone. The peaks around 1355, 1586 and 2691 cm^{-1} can be attributed to the symmetric vibrations from the defected graphite network (D band), the crystalline graphitic regime (G band) and overtone of the D band (2D band) of carbon nanotube, respectively [40]. Upon functionalization, the intensity ratio of the D to G peak increases from 0.2 (± 0.02) to 0.5 (± 0.04). This establishes the presence of newly evolved oxygen functional groups (e.g. $C = O$, C–O, O–$C = O$) upon ozone treatment [44]. By comparing the spread/wicking rate of water in the pristine and functionalised CNT_f samples we could directly observe the transition to a hydrophilic material (Figure S1), and calculate the equivalent contact angle of water using the following equation [40,45]:

$$\frac{S}{S_0}\left[ln\frac{S}{S_0} - 1\right] = -1 + \frac{2\pi r\gamma cos\theta}{3\eta S_0}t \quad (1)$$

Here S and S_0 are the wicking area at time t and 0, respectively, r is the equivalent capillary radius, η the viscosity, γ is the surface tension of the liquid and θ is the equivalent contact angle (for a smooth, flat surface in equilibrium). As shown in Figure S1, the 2 µL droplet remains immobile on the pristine CNT_f fabric, whereas it spreads fast on the functionalized sample, over a few seconds. From the plot of $(S/S_0)(\ln(S/S_0)-1)$ against time (Figure S1f), we estimated the contact angle of water on the functionalized simple to be 67.2°, which confirms the increased hydrophilicity of the functionalized sample.

Fig. 1b-c show the FESEM images of the CNT fibers. As shown in the Fig. 1c, the ultra-long CNT fibers entangle with each other to form the macroscopic fabric. TEM investigations reveals that CNT fibers are a porous network of interconnected CNT bundles with diameter in the range of 8–21 nm (Fig. 1d, e). CNT content and residual catalyst produced during the FC–CVD process can be extracted from thermogravimetric analysis of the CNT fibers (Figure S2).

The CNT_f were deposited on the Si semiconductor surface, which was previously modified with a silanization agent (APTES), and the resulting Si/CNT_f were thermally treated as described in the experimental section. We used electrochemical impedance spectroscopy to analyze the charge transfer at the Si/CNT_f electrodes, using $[Fe(CN)_6]^{4-}/[Fe(CN)_6]^{3-}$ as a redox probe. The charge transfer resistance, R_{ct}, is equal to the diameter of the semicircle extrapolated in the Nyquist plot, in which the real part of the impedance (Z') is plotted along the x-axis and the imaginary part (-Z'') is plotted on the y-axis (each data point is the impedance at one frequency, with frequency decreasing from left to right). [46] Fig. 2A shows the Nyquist plots of Si/CNT_f and silanized Si. The R_{ct} values obtained after fitting to their equivalent circuits (see Fig. 2B) are collected in Table 1. In the absence of irradiation, high impedance values were observed for Si/CNT_f (gray squares in the figure) and a large R_{ct} of 303 kΩ cm^{-2} was found. A 20-fold decrease in the impedance at 1 Hz (lowest frequency applied with corresponds with the far-right data point of the spectra) and a 40-fold reduction in the charge transfer resistance (see Table 1) was achieved upon light irradiation of the Si/CNT_f photoelectrode (red squares). The silanized Si semiconductor (red triangles in Fig. 2A) exhibited a large charge transfer resistance (R_{ct1} in the equivalent circuit indicated in Fig. 2B = 356 kΩ cm^{-2}) upon light irradiation. The smaller semicircle shown in the high frequency region of the Nyquist plot (left side of the plot) can be assigned to lower charge transfer resistance (R_{ct2} in the equivalent circuit indicated in Fig. 2B) of the negatively charged redox probe at the positively charged APTES/electrolyte interface. A bare (non-silanized) Si electrode was also analyzed. Figure S3A shows that the silanization greatly decreased the charge transfer resistance of the semiconductor. Moreover, the R_{ct} of Si/CNT_f fell to half the value of that of a Si/CNT_f photoelectrode which was not thermally treated (Fig. S3B). Therefore, the thermal treatment applied to the photoelectrode, together with silanization, were a successful procedure to enhance the charge transfer.

Table 1
Charge transfer resistance with (ON) and without (OFF) irradiation obtained by fitting the Nyquist plots to the equivalent circuits shown in Fig. 2.

	R_{ct} (kΩ cm^{-2})
Si/CNT_f OFF	303±4
Si/CNT_f ON	7.79±0.08
Silanized Si ON	356±4

3.2. Photoelectrochemical detection of NADH

We investigated the capability of Si/CNT_f electrodes to photooxidize NADH by irradiating the frontal side of the electrode, showing the CNT_f layer. Fig. 3 shows the cyclic voltammograms in the absence and in the presence of irradiation. Upon illumination, a decrease of 0.35 V in the overpotential of NADH oxidation and a 5-fold increase in the current value at about 0.3 V, compared to the measurement without irradiation, were observed. Thus, irradiation significantly reduced the overpotential for NADH oxidation on Si/CNT_f electrodes, without the need of any conventional redox mediator.

We also used linear sweep voltammetry to examine the photoelectrochemical response upon chopped irradiation with and without NADH. The upper limit of the applied potential was 0.4 V vs Ag/AgCl, since more oxidant potentials affected the stability of the photoresponse (Fig. S4). In particular, we observed a gradual increase in the onset potential of NADH photooxidation after voltammetry experiments at higher potential limits. When we swept up to 0.4 V, the overpotential initially increased and after a few scans, the oxidation peak stabilized at around 0.3 V. The shift in the NADH oxidation overpotential correlated with higher charge transfer resistances measured by electrochemical impedance spec-

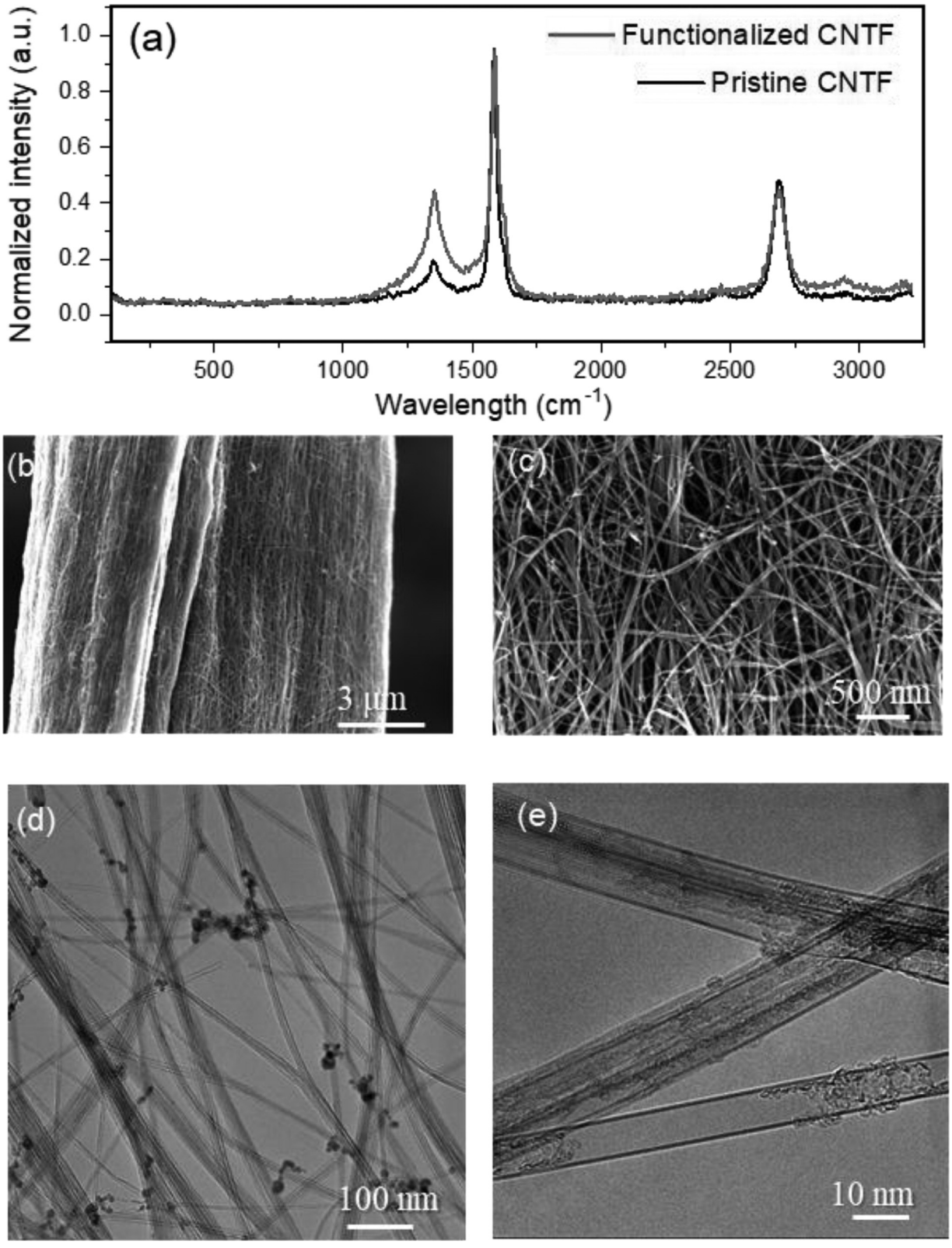


Fig. 1. Characterizations of CNT fibers. (a) Raman spectra of the pristine and ozone treated CNT fibers. (b, c) FESEM and (d, e) TEM images of the CNT fibers.

troscopy experiments (Fig. S5). The increase of the photocurrent in the presence of the NADH was observed at a potential as low as −0.1 V (Fig. 4), while lower currents were obtained in the absence of NADH. The silanized Si electrode exhibited only negligible photocurrents both in phosphate buffer (data not shown) and in the presence of NADH (green trace in Fig. 4). This can be explained by the relatively low conductivity of the Si wafers used (10^{-3}–40 Ω cm), even upon irradiation. Therefore, the presence of CNT_f on the electrode was crucial to detect NADH photooxidation. Herein, the edge plane and functional groups in the CNTf are responsi-

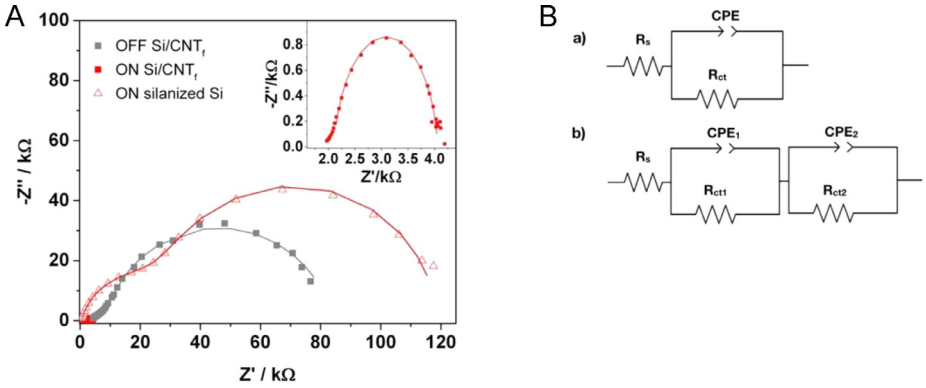


Fig. 2. (A) Nyquist plot curves of Si/CNT_f upon irradiation (red squares, ON) and without irradiation (gray squares, OFF) and a silanized Si semiconductor upon irradiation (red triangles). The lines represent the fit to the equivalent circuits indicated in panel B. Inset in panel A: Magnification of the Nyquist plot of Si/CNT_f upon irradiation. (B) Equivalent circuit of a) Si/CNT_f and b) silanized Si. Conditions: 1 mM $[Fe(CN)_6]^{4-}/[Fe(CN)_6]^{3-}$ solution in 0.1 M phosphate buffer pH 7.5, 0.2 V vs Ag/AgCl, 10^4–1 Hz (10^4–0.1 Hz for the Si semiconductor), 170 mW cm^{-2}. (For interpretation of the references to colour in this figure legend, the reader is referred to the web version of this article.)

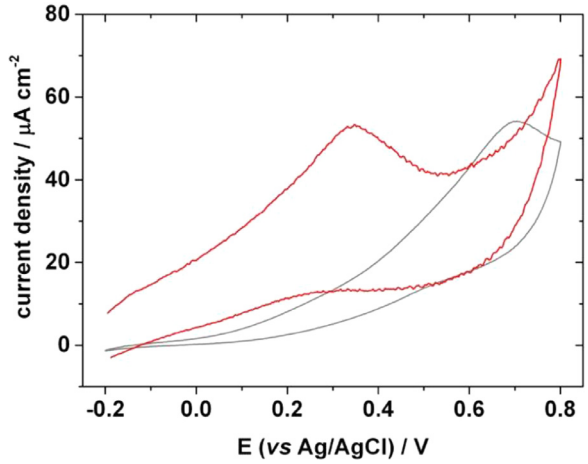


Fig. 3. Cyclic voltammograms of Si/CNT_f upon irradiation (red) and without irradiation (gray) in the presence of 1 mM NADH. Conditions: 0.1 M phosphate buffer pH 7.5, scan rate = 20 mV s^{-1}, 170 mW cm^{-2}. (For interpretation of the references to colour in this figure legend, the reader is referred to the web version of this article.)

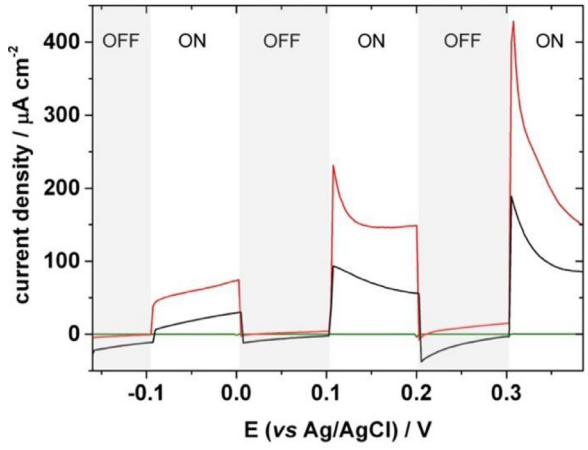


Fig. 4. Linear sweep voltammograms of the Si/CNT_f electrode upon chopped irradiation in the presence (red) and absence of 1 mM NADH (black), and of a silanized Si electrode in the presence of 1 mM NADH (green). Conditions: 0.1 M phosphate buffer pH 7.5, scan rate = 20 mV s^{-1}, 170 mW cm^{-2}. (For interpretation of the references to colour in this figure legend, the reader is referred to the web version of this article.)

ble for the adsorption and catalytic oxidation of NADH [47,48], and the extended conducting network of the CNT_f assists in efficient charge transfer, thereby lowering the overpotential of the NADH oxidation.

To investigate the origin of the NADH photooxidation response, we performed measurements upon back irradiation of the masked (in which the back surface of silicon was covered by PTFE tape) and unmasked Si/CNT_f electrode. When the unmasked electrode was illuminated in this configuration, the cyclic voltammograms remained almost the same as those with frontal irradiation shown above (Fig. S6), whereas for the masked electrode a lower photocurrent was observed and the NADH oxidation peak did not appear at potential lower than 0.4 V (Fig. S7). These results suggest that: (1) the photoelectrocatalytic NADH activity is not caused by photoexcitation of the CNT_f because it occurred even though CNT_f were not directly irradiated by the back illumination; (2) the photoexcitation of Si is indeed required because NADH oxidation at lower overpotential was not measured with the masked electrode; (3) the photoexcitation of Si is not the rate limiting step of the overall photoelectrocatalytic process, as the photocurrent of the unmasked electrode showing a larger Si surface exposed to back irradiation (≈0.8 cm^2) and the masked electrode covered by the CNT_f and PTFE tape (except from $a \approx 0.1$ cm^2 around the CNT_f) upon frontal irradiation were almost equal. As the transmittance of CNT_f is almost 0% (Fig. S8), the Si surface covered by them was not exposed to light and therefore we discarded a hypothetical photoexcitation of Si beneath CNT_f.

To further investigate the role of CNT_f on the NADH photooxidation, we studied the photoresponse of a FTO-based electrode (FTO/CNT_f), which possesses a lower resistivity than that of Si, by linear sweep voltammetry with chopped light. The FTO/CNT_f electrodes showed a NADH oxidation wave at 0.53 V and a greater oxidation current than the bare FTO electrode, but we did not observe any enhancement in the current density upon irradiation (Fig. S9). Furthermore, we showed above that R_{ct} for Si decreased after CNT_f deposition, which means that CNT_f increase the charge transfer at the electrode. Consequently, the photoelectrochemical response of Si/CNT_f electrodes can only be due to the photoexcitation of Si and the efficient charge transfer provided by the CNT_f.

On the basis of such notable photocurrent values achieved at low overpotential with Si/CNT_f electrodes, we studied the influence of NADH concentration on the photoresponse. Since the NADH oxidation photocurrent increased gradually with the applied potential up to ca. 0.30 V, photoelectrochemical experiments were performed at 0.2 V to improve the signal-to-noise ratio, while min-

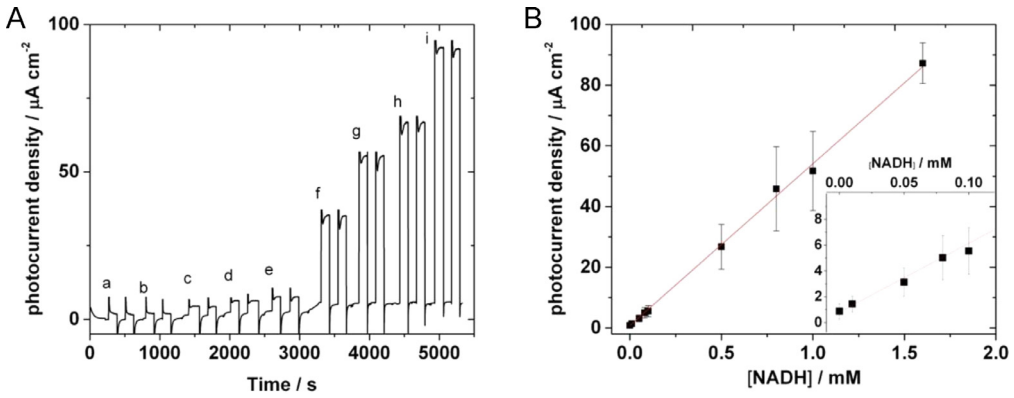


Fig. 5. (A) Photocurrent response of Si/CNT_f to increasing concentrations of NADH (a: blank, b: 0.010 mM, c: 0.050 mM, d: 0.080 mM, e: 0.100 mM, f: 0.500 mM, g: 0.800 mM, h: 1 mM, i: 1.6 mM). (B) Calibration plot (n = 3 electrodes) (photocurrent density (μA cm^{-2}) = 53.7 [NADH] (mM) + 0.566; R^2 = 0.998). Conditions: 0.1 M phosphate buffer pH 7.5, E = 0.2 V vs Ag/AgCl, 170 mW cm^{-2}.

Table 2
Performance comparison of PEC approaches for NADH determination.

Photoelectrode	Sensitivity (μA cm^{-2} mM^{-1})	Linear range (μM)	Refs.
FTO/ZnO/$CsPbBr_3$	15	0.1 - 250	[18]
Si/InGaN/GaN nanowires	91	5 - 50	[20]
FTO/Polydopamine–Nile Blue/Fe_2O_3	5	100 - 2000	[21]
Glassy carbon/$CuWO_4$ nanoplates	140 μA mM^{-1} [a]	10 - 50	[22]
ITO/dopamine-TiO_2	2	0.5 - 120	[23]
Glassy carbon/raspberry shaped ZnO-Au nanostructures	5	1 - 7	[24]
Si/CNT_f	54	50 - 1600	This work

a unknown geometric area of the electrode.

imizing the effect of possible interferences. Fig. 5 shows the results of the experiments in a range of NADH concentrations between 50 μM and 1.6 mM. Two repeated irradiation cycles were performed for each concentration. The photocurrent density (j) linearly increased with NADH concentration in the range measured according to the following equation: j (μA cm^{-2}) = 53.7 [NADH] (mM) + 0.566. The fit yielded a R^2 = 0.998, for 3 independent electrodes. A high sensitivity of 54 ± 12 μA cm^{-2} mM^{-1} was obtained. The detection limit was calculated to be 1 ± 0.7 μM. The Si/CNT_f electrodes showed a broader linear range than most photoelectrochemical approaches reported so far for NADH oxidation and one of the highest sensitivities (Table 2) [18,20–24]. We have found one system in the literature that incorporates a n-type silicon semiconductor as electrode substrate [20], although it does not act as light absorbing material as in our Si/CNT_f system does. After the irradiation cycle and photoelectrochemical NADH oxidation, the initial current (in the dark) is recovered fast and the electrode can be further used. It should be noted that the ON–OFF photochronoamperometric experiments yielded a capacitive discharge when switching the light on. This process is attributed to the absorption of counter-ions when the light is off that are released upon illumination and its concomitant conduction increase. Very small relative standard deviations (<2% for all tests performed) were found for 2 irradiation cycles on the same electrode. The stability of the electrode was further studied for a larger number of repeated irradiation cycles (Fig. 6). 95% of the initial photocurrent was retained after 25 cycles, which proved excellent repeatability. Such electrode stability can be attributed to the reversible redox nature of the catalytic sites in the CNT fiber as well as absence of electrode passivation from the strong adsorption of the NAD^+ produced during NADH oxidation, which is very common for other carbon-based electrodes [49–51]. The high sensitivity achieved also seems to support the absence of such passivation and parasitic reactions. This was also aided by the low potential applied for NADH detection that excludes typical interferences appearing at higher potential values.

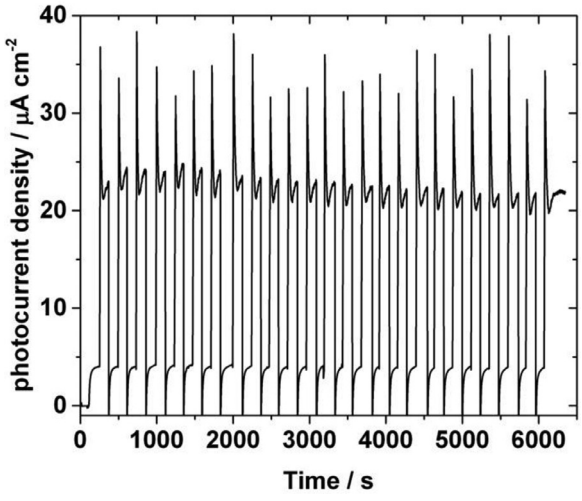


Fig. 6. Stability of the photocurrent response of the Si(APTES)/CNT_f electrode for 25 consecutive measurements (2 min irradiation cycles) in the presence of 0.5 mM NADH. Conditions: 0.1 M phosphate buffer pH 7.5, E = 0.2 V vs Ag/AgCl, 170 mW cm^{-2}.

Conclusions

In this study, we have shown visible-light-triggered detection of NADH using a n-type silicon semiconductor and carbon nanotube fibers. We have demonstrated that the NADH photooxidation signal is generated by the photoexcitation of silicon and the effective charge transfer of CNT_f. The presence of CNT_f is crucial to provide the catalytic sites for NADH oxidation and, to the best of our knowledge, this is the first time they have been applied in a photoelectrocatalytic system for NADH detection. The Si/CNT_f photoelectrodes allowed NADH determination at low potential (0.2 V vs Ag/AgCl) in a broad linear range of 50 μM −1 mM with high

sensitivity. Moreover, the photoelectrodes displayed excellent stability for repetitive NADH detection, which confirms the reversible nature of the CNT_f redox sites and the absence of parasitic reactions to produce catalytic poisons fouling the surface. These results contribute to the development of light-switchable NADH sensors or biosensors by combination with NADH-dependent enzymes.

Credit author statement

Madrid, 4th February 2021

Dear Editor,

All authors have seen and approved the final version of the manuscript being submitted, and this manuscript has not been previously published by any of the authors and/or is not under consideration for publication in another journal at the time of submission.

Yours sincerely,

Dr. Antonio L. De Lacey

Declaration of Competing Interest

The authors declare that they have no known competing financial interests or personal relationships that could have appeared to influence the work reported in this paper.

The authors declare the following financial interests/personal relationships which may be considered as potential competing interests.

Acknowledgements

M.B. acknowledges funding from the European Union's Horizon 2020 research and innovation program under the Marie Skłodowska-Curie grant agreement No. 713366. A.D.L., M.R and J.J.V. thank the "Comunidad de Madrid" for its support to the FotoArt-CM project (S2018/NMT-4367) through the Program of R&D activities between research groups in Technologies 2018, co-financed by European Structural Funds. J.J.V. is grateful for generous financial support provided by the European Union Horizon 2020 Program under grant agreement 678565 (ERC-STEM) and by the MINECO (RyC-2014-15115, HYNANOSC RTI2018-099504-A-C22).

Supplementary materials

Supplementary material associated with this article can be found, in the online version, at doi:10.1016/j.electacta.2021.138071.

References

[1] H. Jaegfeldt, T. Kuwana, G. Johansson, Electrochemical stability of catechols with a pyrene side chain strongly adsorbed on graphite electrodes for catalytic oxidation of dihydronicotinamide adenine dinucleotide, J. Am. Chem. Soc. 105 (1983) 1805–1814, doi:10.1021/ja00345a021.

[2] G.D. Birkmayer, N.A.D.H. The energizing coenzyme, in: a keats good health guide, 1993: pp. 1–22.

[3] F.S. Omar, N. Duraisamy, K. Ramesh, S. Ramesh, Conducting polymer and its composite materials based electrochemical sensor for Nicotinamide Adenine Dinucleotide (NADH), Biosens. Bioelectron. 79 (2016) 763–775, doi:10.1016/j.bios.2016.01.013.

[4] G.D. Birkmayer, the Biological Hydrogen NADH, The Secret of Our Life Energy, Basic Health Publications, Inc., 2009.

[5] P. Theurey, N.M.C. Connolly, I. Fortunati, E. Basso, S. Lauwen, C. Ferrante, C. Moreira Pinho, A. Joselin, A. Gioran, D. Bano, D.S. Park, M. Ankarcrona, P. Pizzo, J.H.M. Prehn, Systems biology identifies preserved integrity but impaired metabolism of mitochondria due to a glycolytic defect in Alzheimer's disease neurons, Aging Cell 18 (2019) e12924, doi:10.1111/acel.12924.

[6] A.R. Hipkiss, Alzheimer's disease and dysfunctional glycolysis; similar effects of too much and too little, Aging Dis. 10 (2019) 1328–1331, doi:10.14336/AD.2019.0611.

[7] G.S. McElroy, C.R. Reczek, P.A. Reyfman, D.S. Mithal, C.M. Horbinski, N.S. Chandel, NAD+ regeneration rescues lifespan, but not ataxia, in a mouse model of brain mitochondrial complex I dysfunction, Cell Metab. 32 (2020) 301–308 e6, doi:10.1016/j.cmet.2020.06.003.

[8] S.-Y. Kim, B.M. Cohen, X. Chen, S.E. Lukas, A.K. Shinn, A.C. Yuksel, T. Li, F. Du, D. Öngür, Redox dysregulation in schizophrenia revealed by in vivo NAD+/NADH measurement, Schizophr. Bull. 43 (2017) 197–204, doi:10.1093/schbul/sbw129.

[9] A.C. Andreazza, L. Shao, J.-F. Wang, L.T. Young, Mitochondrial complex I activity and oxidative damage to mitochondrial proteins in the prefrontal cortex of patients with bipolar disorder, Arch. Gen. Psychiatry 67 (2010) 360–368, doi:10.1001/archgenpsychiatry.2010.22.

[10] V.B. Ritov, E.V. Menshikova, D.E. Kelley, High-performance liquid chromatography-based methods of enzymatic analysis: electron transport chain activity in mitochondria from human skeletal muscle, Anal. Biochem. 333 (2004) 27–38, doi:10.1016/j.ab.2004.05.014.

[11] T.S. Blacker, Z.F. Mann, J.E. Gale, M. Ziegler, A.J. Bain, G. Szabadkai, M.R. Duchen, Separating NADH and NADPH fluorescence in live cells and tissues using FLIM, Nat. Commun. 5 (2014) 3936, doi:10.1038/ncomms4936.

[12] S.Y. Park, S.A. Yoon, Y. Cha, M.H. Lee, Recent advances in fluorescent probes for cellular antioxidants: detection of NADH, hNQO1, H2S, and other redox biomolecules, Coord. Chem. Rev. 428 (2021) 213613, doi:10.1016/j.ccr.2020.213613.

[13] A. Devadoss, L. Dennany, C. Dickinson, T.E. Keyes, R.J. Forster, Highly sensitive detection of NADH using electrochemiluminescent nanocomposites, Electrochem. Commun. 19 (2012) 43–45, doi:10.1016/j.elecom.2012.03.003.

[14] Y. Li, X. Yang, F. Yang, Y. Wang, P. Zheng, X. Liu, Effective immobilization of Ru(bpy)32+ by functional composite phosphomolybdic acid anion on an electrode surface for solid-state electrochemiluminescene to sensitive determination of NADH, Electrochim. Acta 66 (2012) 188–192, doi:10.1016/j.electacta.2012.01.087.

[15] H. Chen, X. Liu, C. Yin, W. Li, X. Qin, C. Chen, A dual-signal output ratiometric electrochemiluminescent sensor for NADH detection, Analyst 144 (2019) 5215–5222, doi:10.1039/C9AN00758J.

[16] S. Han, T. Du, H. Jiang, X. Wang, Synergistic effect of pyrroloquinoline quinone and graphene nano-interface for facile fabrication of sensitive NADH biosensor, Biosens. Bioelectron. 89 (2017) 422–429, doi:10.1016/j.bios.2016.04.092.

[17] M. Revenga-Parra, C. Gómez-Anquela, T. García-Mendiola, E. Gonzalez, F. Pariente, E. Lorenzo, Grafted Azure A modified electrodes as disposable β-nicotinamide adenine dinucleotide sensors, Anal Chim Acta 747 (2012) 84–91, doi:10.1016/j.aca.2012.07.043.

[18] Y. Zhu, X. Tong, H. Song, Y. Wang, Z. Qiao, D. Qiu, J. Huang, Z. Lu, $CsPbBr_3$ perovskite quantum dots/ZnO inverse opal electrodes: photoelectrochemical sensing for dihydronicotinamide adenine dinucleotide under visible irradiation, Dalton Trans. 47 (2018) 10057–10062, doi:10.1039/C8DT01790E.

[19] F. Jafari, A. Salimi, A. Navaee, Electrochemical and photoelectrochemical sensing of NADH and ethanol based on immobilization of electrogenerated chlorpromazine sulfoxide onto graphene-CdS quantum dot/ionic liquid nanocomposite, Electroanalysis 26 (2014) 530–540, doi:10.1002/elan.201300508.

[20] M. Riedel, S. Hölzel, P. Hille, J. Schörmann, M. Eickhoff, F. Lisdat, InGaN/GaN nanowires as a new platform for photoelectrochemical sensors – detection of NADH, Biosens. Bioelectron. 94 (2017) 298–304, doi:10.1016/j.bios.2017.03.022.

[21] G.M. Ryu, M. Lee, D.S. Choi, C.B. Park, A hematite-based photoelectrochemical platform for visible light-induced biosensing, J. Mater. Chem. B. 3 (2015) 4483–4486, doi:10.1039/C5TB00478K.

[22] B. Mohanty, K.K. Naik, S. Sahoo, B. Jena, B. Chakraborty, C.S. Rout, B.K. Jena, Efficient photoelectrocatalytic activity of $CuWO_4$ nanoplates towards the oxidation of NADH driven in visible light, ChemistrySelect 3 (2018) 9008–9012, doi:10.1002/slct.201801137.

[23] G.-L. Wang, J.-J. Xu, H.-Y. Chen, Dopamine sensitized nanoporous TiO_2 film on electrodes: photoelectrochemical sensing of NADH under visible irradiation, Biosens. Bioelectron. 24 (2009) 2494–2498, doi:10.1016/j.bios.2008.12.031.

[24] A.K. Samantara, S.Chandra Sahu, B. Bag, B. Jena, B.K. Jena, Photoelectrocatalytic oxidation of NADH by visible light driven plasmonic nanocomposites, J. Mater. Chem. A. 2 (2014) 12677, doi:10.1039/C4TA01349B.

[25] L. Gorton, E. Domínguez, Electrochemistry of NAD(P)+/NAD(P)H, in: Encyclopedia of Electrochemistry, American Cancer Society, 2007, doi:10.1002/9783527610426.bard090004.

[26] A. Radoi, D. Compagnone, Recent advances in NADH electrochemical sensing design, Bioelectrochemistry 76 (2009) 126–134, doi:10.1016/j.bioelechem.2009.06.008.

[27] Jacques. Moiroux, P.J. Elving, Effects of adsorption, electrode material, and operational variables on the oxidation of dihydronicotinamide adenine dinucleotide at carbon electrodes, Anal. Chem. 50 (1978) 1056–1062, doi:10.1021/ac50030a015.

[28] N. Mano, A. Thienpont, A. Kuhn, Adsorption and catalytic activity of trinitrofluorenone derivatives towards NADH oxidation on different electrode materials, Electrochem. Commun. 3 (2001) 585–589, doi:10.1016/S1388-2481(01)00224-7.

[29] A. Maleki, D. Nematollahi, J. Clausmeyer, J. Henig, N. Plumeré, W. Schuhmann, Electrodeposition of catechol on glassy carbon electrode and its electrocatalytic activity toward NADH oxidation, Electroanalysis 24 (2012) 1932–1936, doi:10.1002/elan.201200251.

[30] J. Wang, R.P. Deo, P. Poulin, M. Mangey, Carbon nanotube fiber microelectrodes, J. Am. Chem. Soc. 125 (2003) 14706–14707, doi:10.1021/ja037737j.

[31] L. Viry, A. Derré, P. Garrigue, N. Sojic, P. Poulin, A. Kuhn, Optimized carbon nanotube fiber microelectrodes as potential analytical tools, Anal. Bioanal. Chem. 389 (2007) 499–505, doi:10.1007/s00216-007-1467-9.

[32] W.-W. Zhao, J.-J. Xu, H.-Y. Chen, Photoelectrochemical bioanalysis: the state of the art, Chem. Soc. Rev. 44 (2015) 729–741, doi:10.1039/C4CS00228H.

[33] Y. Zang, J. Fan, Y. Ju, H. Xue, H. Pang, Current advances in semiconductor nanomaterial-based photoelectrochemical biosensing, Chem. Eur. J. 24 (2018) 14010–14027, doi:10.1002/chem.201801358.
[34] W.-.W. Zhao, J.-.J. Xu, H.-.Y. Chen, Photoelectrochemical enzymatic biosensors, Biosens. Bioelectron. 92 (2017) 294–304, doi:10.1016/j.bios.2016.11.009.
[35] M. del Barrio, G. Luna-López, M. Pita, Enhancement of biosensors by implementing photoelectrochemical processes, Sensors 20 (2020) 3281, doi:10.3390/s20113281.
[36] Y. Zang, J. Lei, H. Ju, Principles and applications of photoelectrochemical sensing strategies based on biofunctionalized nanostructures, Biosens. Bioelectron. 96 (2017) 8–16, doi:10.1016/j.bios.2017.04.030.
[37] Y. Wang, M. Zu, X. Zhou, H. Lin, F. Peng, S. Zhang, Designing efficient TiO2-based photoelectrocatalysis systems for chemical engineering and sensing, Chem. Eng. J. 381 (2020) 122605, doi:10.1016/j.cej.2019.122605.
[38] E. Senokos, V. Reguero, J. Palma, J.J. Vilatela, R. Marcilla, Macroscopic fibres of CNTs as electrodes for multifunctional electric double layer capacitors: from quantum capacitance to device performance, Nanoscale 8 (2016) 3620–3628, doi:10.1039/C5NR07697H.
[39] V. Reguero, B. Alemán, B. Mas, J.J. Vilatela, Controlling carbon nanotube type in macroscopic fibers synthesized by the direct spinning process, Chem. Mater. 26 (2014) 3550–3557, doi:10.1021/cm501187x.
[40] E. Senokos, M. Rana, C. Santos, R. Marcilla, J.J. Vilatela, Controlled electrochemical functionalization of CNT fibers: structure-chemistry relations and application in current collector-free all-solid supercapacitors, Carbon N Y 142 (2019) 599–609, doi:10.1016/j.carbon.2018.10.082.
[41] M. Krämer, M. Pita, J. Zhou, M. Ornatska, A. Poghossian, M.J. Schöning, E. Katz, Coupling of biocomputing systems with electronic chips: electronic interface for transduction of biochemical information, J. Phys. Chem. C. 113 (2009) 2573–2579, doi:10.1021/jp808320s.
[42] S. Grau, S. Berardi, A. Moya, R. Matheu, V. Cristino, J.J. Vilatela, C.A. Bignozzi, S. Caramori, C. Gimbert-Suriñach, A. Llobet, A hybrid molecular photoanode for efficient light-induced water oxidation, Sustain. Energy Fuels 2 (2018) 1979–1985, doi:10.1039/C8SE00146D.
[43] C. Jarne, L. Paul, J.C. Conesa, S. Shleev, A.L. De Lacey, M. Pita, Underpotential photoelectrooxidation of water by SnS_2 −laccase Co-catalysts on nanostructured electrodes with only visible-light irradiation, ChemElectroChem 6 (2019) 2755–2761, doi:10.1002/celc.201900360.
[44] D. Iglesias, E. Senokos, B. Alemán, L. Cabana, C. Navío, R. Marcilla, M. Prato, J.J. Vilatela, S. Marchesan, Gas-phase functionalization of macroscopic carbon nanotube fiber assemblies: reaction control, electrochemical properties, and use for flexible supercapacitors, ACS Appl. Mater. Interfaces 10 (2018) 5760–5770, doi:10.1021/acsami.7b15973.
[45] A. Borhan, K.K. Rungta, An experimental study of the radial penetration of liquids in thin porous substrates, J. Colloid Interface Sci. 158 (1993) 403–411, doi:10.1006/jcis.1993.1272.
[46] A.J. Bard, L.R. Faulkner, Electrochemical Methods: Fundamentals and Applications, 2nd Edition, John Wiley & Sons, 2001 Incorporatedhttps://books.google.es/books?id=hQocAAAAQBAJ.
[47] C.E. Banks, R.G. Compton, Exploring the electrocatalytic sites of carbon nanotubes for NADH detection: an edge plane pyrolytic graphite electrode study, Analyst 130 (2005) 1232–1239, doi:10.1039/B508702C.
[48] A. Martínez-Muíño, M. Rana, J.J. Vilatela, R.D. Costa, Origin of the electrocatalytic activity in carbon nanotube fiber counter-electrodes for solar-energy conversion, Nanoscale Adv. 2 (2020) 4400–4409, doi:10.1039/D0NA00492H.
[49] T.N. Rao, I. Yagi, T. Miwa, D.A. Tryk, A. Fujishima, Electrochemical oxidation of NADH at highly boron-doped diamond electrodes, Anal. Chem. 71 (1999) 2506–2511, doi:10.1021/ac981376m.
[50] F. Pariente, F. Tobalina, G. Moreno, L. Hernández, E. Lorenzo, H.D. Abruña, Mechanistic studies of the electrocatalytic oxidation of NADH and ascorbate at glassy carbon electrodes modified with electrodeposited films derived from 3,4-dihydroxybenzaldehyde, Anal. Chem. 69 (1997) 4065–4075, doi:10.1021/ac970445e.
[51] M. Musameh, J. Wang, A. Merkoci, Y. Lin, Low-potential stable NADH detection at carbon-nanotube-modified glassy carbon electrodes, Electrochem. Commun. 4 (2002) 743–746, doi:10.1016/S1388-2481(02)00451-4.